INTERNATIONAL JOURNAL FOR NUMERICAL METHODS IN FLUIDS
Int. J. Numer. Meth. Fluids 2001; **37**: 837–864 (DOI: 10.1002/fld.190)

A comparison of boundary element and finite element methods for modeling axisymmetric polymeric drop deformation

Russell Hooper[a], Matthijs Toose[b], Christopher W. Macosko[a] and Jeffrey J. Derby[a,*,1]

[a] *Department of Chemical Engineering and Materials Science, Army HPC Research Center, and Minnesota Supercomputing Institute, University of Minnesota, Minneapolis, MN, U.S.A.*
[b] *Rheology Group, Department of Applied Physics, University of Twente, Enschede, Netherlands*

SUMMARY

A modified boundary element method (BEM) and the DEVSS-G finite element method (FEM) are applied to model the deformation of a polymeric drop suspended in another fluid subjected to start-up uniaxial extensional flow. The effects of viscoelasticity, via the Oldroyd-B differential model, are considered for the drop phase using both FEM and BEM and for both the drop and matrix phases using FEM. Where possible, results are compared with the linear deformation theory. Consistent predictions are obtained among the BEM, FEM, and linear theory for purely Newtonian systems and between FEM and linear theory for fully viscoelastic systems. FEM and BEM predictions for viscoelastic drops in a Newtonian matrix agree very well at short times but differ at longer times, with worst agreement occurring as critical flow strength is approached. This suggests that the dominant computational advantages held by the BEM over the FEM for this and similar problems may diminish or even disappear when the issue of accuracy is appropriately considered. Fully viscoelastic problems, which are only feasible using the FEM formulation, shed new insight on the role of viscoelasticity of the matrix fluid in drop deformation. Copyright © 2001 John Wiley & Sons, Ltd.

KEY WORDS: axisymmetric polymeric drop deformation; boundary element method; finite element method; modeling

1. INTRODUCTION

Modeling the transient deformation of an immiscible polymeric drop within a polymeric fluid in shear or extensional flow is of great interest for better understanding the effects of processing on the morphology of a polymeric composite. There is much current interest in such

* Correspondence to: Department of Chemical Engineering and Materials Science, Institute of Technology, University of Minnesota, 151 Amundson Hall, 421 Washington Avenue, SE, Minneapolis, MN 55455-0132, U.S.A.
[1] E-mail: derby@tc.umn.edu

Received 13 January 2001
Revised 28 February 2001

composites, since the blending of a small amount of appropriate specialty polymer(s) to a common bulk polymer can produce a new material with desirable properties. The final properties of the product made from a polymeric blend are highly dependent on the morphology of the dispersed phase(s), i.e. the size, shape and orientation of droplets. For example, the permeability can be tailored by proper control of blend morphology [1–3]. Computational models can play an important role in the study of these systems, if robust and accurate methods are available. This motivates the study presented here. First, we present a comparison of two powerful numerical methods, the boundary element method (BEM) and the finite element method (FEM), to model the dynamics of polymeric drop elongation in uniaxial extensional flows. We directly compare the performance of these methods on several problems of polymeric drops within Newtonian fluid. Second, we also present FEM computations of polymeric drop extension in a polymeric matrix. Such results have not yet been obtained in prior studies and shed new insight to the behavior of these systems.

Drop deformation has received considerable attention, beginning with the seminal work of Taylor [4]. Taylor's original contribution was to provide an analytical solution, accurate to first-order in deformation, describing the deformation of a Newtonian drop sheared in another Newtonian fluid. The theory was refined [5,6] and extended to other situations, such as viscous drops surrounded by a viscoelastic shell [7] and double concentric viscous drops [8]. Excellent reviews of these contributions can be found in Rallison [9] and Stone [10]. An extensive study of the effects of the interface properties of viscous drops on the rheology of a dilute emulsion was performed by Oldroyd [11,12]. Palierne [13,14] recently extended the work of Oldroyd to described viscoelastic drops with interfacial tension. More recently, Delaby *et al.* [15–17] have successfully applied the linear emulsion theory of Palierne to uniaxial extensional flow. A different approach was taken by Roscoe [18] who used the work of Jeffery [19] on solid ellipsoidal particles in a viscous flow to describe the deformation of viscoelastic particles. While representing significant advances, the analytical solutions for drop behavior described in these works are limited to small deformations.

The deformation of Newtonian drops in viscous extensional flows at low Reynolds number was first studied numerically by Youngren [20] using BEM. For drops composed of Newtonian fluids alone, this method involves only quantities at the boundaries and thereby reduces the dimension of the spatial computational domain by one. The method has since been used extensively by others to simulate the behavior of Newtonian drops in simple flow fields. Recent studies have tackled more complicated flow problems and have incorporated additional physical phenomena, e.g. the breakup of drops [21], the effects due to surfactants [22], and elasticity of the interface [23]. Recently, the BEM was also used to simulate concentrated emulsions of viscous drops in shear flow [24,25] and double concentric viscous drops [8].

Similar numerical studies of drop behavior involving polymeric fluids are much fewer in number. Toose *et al.* [26–28] were among the first to model polymeric drop deformation in a Newtonian matrix using the BEM. A finite difference scheme was used by Ramaswamy and Leal [29,30] to study steady state drop deformations where either the drop or matrix was viscoelastic. The first application of the FEM to transient, free-surface flows involving viscoelasticity was that of Keunings [31]; this approach was subsequently applied to study breakup of viscoelastic threads in a viscoelastic matrix [32], deformation of an inviscid inclusion in a viscoelastic extensional flow [33], and drop deformation in uniaxial extensional flow where one phase is viscoelastic and the other Newtonian [17].

In the work presented here, we model viscoelastic drop deformation in start-up uniaxial extensional flow using two different methods, the FEM and the BEM. Specifically, we apply a framework similar to that Keunings [31] and employ the robust DEVSS-G FEM [34,35] to develop a new method for describing viscoelastic moving-boundary flows. We also directly employ the BEM developed by Toose [27] to compute the extension of viscoelastic drops. This collaborative study represents an opportunity for a direct comparison of two very different methods. Such head-to-head comparisons of methods are relatively infrequent, since each method involves a substantial investment in code development for modeling problems of this complexity. Section 2 contains a description of the model system and the governing equations for the viscoelastic drop deformation problem. Sections 3 and 4 are devoted to the numerical methods (DEVSS-G FEM and BEM) used to obtain solutions to the governing equations. Results and conclusions are presented in Sections 5 and 6 respectively. The advantages and disadvantages of each method are assessed, and new results are presented for viscoelastic drop deformations beyond the linear regime and for cases of viscoelastic drop and matrix fluids.

2. PROBLEM STATEMENT

Shown schematically in Figure 1 is an isotropic, axisymmetric, non-Newtonian drop suspended in an unbounded non-Newtonian matrix, which is subjected to a linear elongational flow at $t = 0$, where t denotes time. The drop center is placed at the stagnation point of the external flow field, v^{∞}, which is defined by

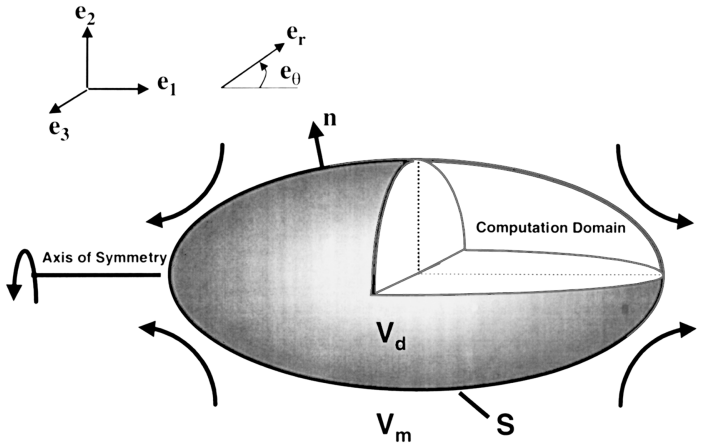

Figure 1. Schematic of an axisymmetric drop suspended in an unbounded, neutrally buoyant matrix subjected to uniaxial extension at $t = 0$. Both phases (drop and matrix) are viscoelastic, in general, and the drop is initially spherical with radius R_0.

$$v_1^\infty = \dot{\epsilon} x_1, \qquad v_2^\infty = -\frac{1}{2}\dot{\epsilon} x_2, \qquad v_3^\infty = -\frac{1}{2}\dot{\epsilon} x_3 \tag{1}$$

where v_j^∞ is the jth component of the velocity field with respect to a Cartesian coordinate frame, $\{\boldsymbol{e}_1, \boldsymbol{e}_2, \boldsymbol{e}_3\}$, and $\dot{\varepsilon}$ is the strain rate of the extensional flow. The center of the drop is located at the stagnation point of the external flow field, $\boldsymbol{x} = \boldsymbol{0}$. The domains occupied by the non-Newtonian drop and matrix are denoted by V_d and V_m respectively. Along the interface, S, between the domains, there acts a constant interfacial tension, σ. The fluid is incompressible, and buoyancy is considered to be absent, i.e. the densities of drop and matrix are assumed to be equal. The initial drop configuration is taken to be a sphere with radius R_0.

The governing equations for the system described above include momentum and mass conservation, a constitutive equation relating stresses to material deformations, a kinematic relation describing the movement of the drop boundary, and appropriate initial and boundary conditions. In general, momentum conservation can be expressed as [36]

$$\rho\left(\frac{\partial \boldsymbol{v}'}{\partial t'} + \boldsymbol{v}' \cdot \nabla' \boldsymbol{v}'\right) = \nabla' \cdot \boldsymbol{T}' + \rho g \boldsymbol{e}_g \tag{2}$$

where primes denote dimensional quantities, ρ is the fluid density, and g and $\boldsymbol{e}_\mathrm{g}$ are the magnitude and direction of gravity respectively. Assuming fluid incompressibility, mass conservation is given by

$$\nabla' \cdot \boldsymbol{v}' = 0 \tag{3}$$

To recast the above using dimensionless variables, lengths are scaled by the initial drop radius R_0, time by the inverse strain rate, $1/\dot{\epsilon}$, and stresses by the characteristic scale of the external flow, $\mu_\mathrm{m}\dot{\epsilon}$, with μ_m representing the viscosity of the matrix phase. The non-dimensional momentum and mass balances are then given by

$$\frac{\rho R_0^2 \dot{\epsilon}}{\mu_\mathrm{m}}\left(\frac{\partial \boldsymbol{v}}{\partial t} + \boldsymbol{v} \cdot \nabla \boldsymbol{v}\right) = \nabla \cdot \boldsymbol{T} + \frac{\rho g R_0}{\mu_\mathrm{m}\dot{\epsilon}} \boldsymbol{e}_g \tag{4}$$

$$\nabla \cdot \boldsymbol{v} = 0 \tag{5}$$

respectively.

The dimensionless group on the left of Equation (4) is the Reynolds number, Re, which is very small for viscous polymeric drops of small radii, e.g. for $R_0 = O(10^{-5}$ m), the $Re = O(10^{-10})$. The dimensionless group on the right of Equation (4) is the ratio of Re/Fr, with Fr as the Froude number, and is $O(10^{-4})$. These scaling arguments suggest simplification by neglecting inertia and gravity, thereby reducing Equation (4) to the following

$$\nabla \cdot \boldsymbol{T} = 0 \tag{6}$$

Together, Equations (5) and (6) describe the behavior of the drop and matrix fluids during flow. It remains to specify the constitutive behavior, as well as boundary and initial conditions.

Several integral and differential constitutive equations have been developed to relate the state of stress in the fluid to current and past deformations and deformation rates [37,38]. In this paper, we employ the Oldroyd-B model, although the numerical methods discussed later can be extended to quite general rheological models. The Oldroyd-B model finds its origin in polymer rheology and contains three parameters: a Newtonian solvent viscosity μ_s, a polymer relaxation time λ, and a polymer contribution to the viscosity μ_p [37]. The total fluid viscosity is the sum of solvent and polymer contributions, i.e. $\mu = \mu_s + \mu_p$. Consistent with this splitting into polymer and Newtonian solvent contributions, the total stress state of the fluid is expressed as

$$\boldsymbol{T} = -P\boldsymbol{I} + p_s\dot{\boldsymbol{\gamma}} + \boldsymbol{\tau} \tag{7}$$

where P is the isotropic pressure, $\boldsymbol{I}$ is the identity tensor, $\dot{\boldsymbol{\gamma}} = (\nabla\boldsymbol{v} + \nabla\boldsymbol{v}^T)$ is the rate-of-strain tensor, and $p_s = \mu_s/\mu$ is the solvent viscosity ratio. The extra-stress tensor, $\boldsymbol{\tau}$, in Equation (7) is given implicitly by

$$\boldsymbol{\tau} + De\overset{\nabla}{\boldsymbol{\tau}} = p_p\dot{\boldsymbol{\gamma}} \tag{8}$$

where $De = \dot{\epsilon}\lambda$ is the Deborah number, which is a time-scale ratio of the fluid response time, λ, to that imposed by the extensional flow, $1/\dot{\epsilon}$, and $p_p = \mu_p/\mu$ is the polymer viscosity ratio. In Equation (8) $\overset{\nabla}{\boldsymbol{\tau}}$ is the upper-convected derivative of the extra stress tensor and is defined as [37]

$$\overset{\nabla}{\boldsymbol{\tau}} \equiv \frac{\partial\boldsymbol{\tau}}{\partial t} + \boldsymbol{v}\cdot\nabla\boldsymbol{\tau} - \nabla\boldsymbol{v}^T\cdot\boldsymbol{\tau} - \boldsymbol{\tau}\cdot\nabla\boldsymbol{v} \tag{9}$$

The Oldroyd-B model is one of the simplest non-linear, time-dependent differential constitutive equations. It attributes to the fluid a constant viscosity (no shear thinning) and first normal stresses that increase quadratically with shear rate [38]. Equation (7) reduces to an upper convected Maxwell (UCM) model when $p_s = 0$, and a Newtonian fluid is obtained when $De = 0$. Conversely, elastic solid behavior is approached as $De \to \infty$. Hence, the Deborah number reflects departure from Newtonian behavior, with elastic effects becoming more pronounced for larger De. While seeming to imply application to polymer solutions, the Oldroyd-B relation can be successfully employed for polymer melts so long as the parameters are fit properly to experimental data. To achieve a good fit to viscometric data, a spectrum of relaxation times is typically required [38]. For each relaxation mode, an equation of the form of Equation (8) applies, and the total stress response is the sum of each contribution. In this work, only a single relaxation time is considered; additional modes could be incorporated in a straightforward manner though with increased computational expense.

The above equations apply to both the drop and matrix fluid; we denote the drop phase parameters by a subscript d and those of the exterior matrix by subscript m. Thus, the Oldroyd-B parameters for the drop are the Deborah number, $De_d = \lambda_d\dot{\epsilon}$, the total viscosity μ_d, made up of polymer, μ_{pd}, and solvent, μ_{sd}, contributions, and viscosity ratios $p_{pd} = \mu_{pd}/\mu_d$ and

$p_{sd} = 1 - p_{pd}$. The drop and matrix phases are related by the viscosity ratio, $p = \mu_d/\mu_m$, and the elasticity ratio, $De_\tau = De_d/De_m = \lambda_d/\lambda_m$.

The system of partial differential equations defined by Equations (5) and (6) require initial conditions and boundary conditions. One boundary condition is specified by applying the following nondimensional force balance [39] at the drop boundary, S (see Figure 1)

$$\frac{\mu_m R_0 \dot{\epsilon}}{\sigma} [\boldsymbol{n} \cdot \boldsymbol{T}]_s - \kappa \boldsymbol{n} = \boldsymbol{0} \tag{10}$$

where $\boldsymbol{n}$ is a unit vector that is directed outward from the drop and normal to its surface S, κ is the dimensionless mean surface curvature and $[\cdot]_S$ denotes the jump of the quantity between the brackets over the interface S counted in the direction $\boldsymbol{n}$. Equation (10) expresses a jump in normal stress due to capillarity and implies continuity of tangential stress across the drop boundary. The dimensionless group on the left side of Equation (10) is the capillary number, $Ca = \mu_m R_0 \dot{\epsilon}/\sigma$, which represents the ratio between viscous and interfacial stresses at the interface. This parameter has special meaning in the drop extension problem, namely the exterior flow strengths can be classified as supercritical or subcritical depending on whether Ca exceeds a critical value, Ca_c. When $Ca > Ca_c$, viscous stresses dominate over interfacial stresses, and no steady drop shape can be attained under the given flow conditions.

A kinematic constraint is also imposed at the drop interface, S, which defines a material surface. The trajectories of these points are followed using a Lagrangian representation of their velocities:

$$\boldsymbol{u}(\boldsymbol{x}) - \dot{\boldsymbol{x}} = \boldsymbol{0}, \quad \text{for all } \boldsymbol{x} \in S(t) \tag{11}$$

where the dot denotes a material time derivative. This boundary condition Equation (11) is implemented by representing the drop boundary by a scalar function, $F = 0$. Evolution of the moving surface is then related to the local velocity field by requiring the material derivative of F to be zero [40]

$$\frac{\partial F}{\partial t} + \boldsymbol{v} \cdot \nabla F = 0 \tag{12}$$

Far away from the drop, the exterior flow approaches that of pure uniaxial extension

$$\boldsymbol{v} \to \boldsymbol{v}^\infty, \quad \text{as } |\boldsymbol{x}| \to \infty \tag{13}$$

Here, we assume axisymmetry, so that a single quadrant of the problem can be considered. The following boundary conditions are imposed along the symmetry planes corresponding to the drop's extensional axis ($y = z = 0$) and mid-plane ($x = 0$)

$$\boldsymbol{n} \cdot \boldsymbol{v} = 0 \tag{14}$$

$$\boldsymbol{n} \cdot \boldsymbol{T} \cdot \boldsymbol{t} = 0 \tag{15}$$

Physically, Equation (14) enforces no fluid flow across the planes of symmetry, while Equation (15) prevents any tangential stresses from acting along the planes.

For the evolution Equations (8) and (12), initial conditions are required. For the interface, S, it is natural to start with a spherical shape. The extra stress tensor, $\boldsymbol{\tau}$, is assigned an isotropic stress distribution

$$\boldsymbol{\tau}(0) = Q\boldsymbol{I} \tag{16}$$

with Q constant and equal to zero. This corresponds to a stress state where the fluid is initially everywhere at rest.

3. DEVSS-G FINITE ELEMENT METHOD

The simulation of viscoelastic fluid flow by the FEM has progressed considerably over the past decade. In short, past research has found that the traditional Galerkin FEM readily breaks down for problems having even small amounts of viscoelasticity (i.e. small De). For creeping flows, this is due in part to the onset and propagation of mesh-sized instabilities, which occur as the governing equations change type from elliptic to hyperbolic [41,42]. This occurs as De is increased due to approximation errors in the numerical method. Another issue which plagued early viscoelastic finite element simulations and which has since been explained is the existence of a compatibility constraint or inf–sup condition for the velocity and extra stress unknowns [34]. Similar to the LBB condition for velocities and pressures in purely Newtonian problems, the discrete representation of extra stresses is required at more nodes internal to an element than the number of velocity nodes along the element boundary. A final complicating feature of viscoelastic flows is the transport of momentum by convection arising from the constitutive behavior of the fluid, i.e. the $\boldsymbol{v}\cdot\nabla\boldsymbol{\tau}$ term in Equation (9). While only creeping flows are considered in this work, the problems associated with momentum convection are analogous to those encountered in flows where inertial effects are significant [43]. As De is increased, convective momentum transport plays an increasingly important role, and Galerkin FEM, which is known to suffer from oscillations when applied to strong convective flows, no longer gives credible results. Taken together, these issues comprise what is commonly called the 'high Weissenberg number problem', where for steady flows, the Weissenberg number is analogous to the Deborah number in transient flows.

To deal with these issues, several variations of the FEM have been devised. An excellent chronology with details of each variation is provided in the recent review by Baaijens [34]. For reasons discussed at length in the review, a variant of FEM known as the discrete elasticviscous stress-splitting method with continuous interpolation of the velocity gradient, hereafter referred to simply as the DEVSS-G FEM, is adapted to the drop deformation problem considered here. The method is based on the idea of a mixed formulation which splits the viscous and elastic components of stress and introduces a continuous approximation, G, of the numerically discontinuous velocity gradient tensor, $\nabla\boldsymbol{v}$. The numerical difference between G and $\nabla\boldsymbol{v}$ is used to preserve the elliptic character of the momentum equation and thereby circumvent the inf–sup condition for velocity and extra stress. Moreover, G is also used in

place of $\nabla \boldsymbol{v}$ in Equation (9). Streamline upwinding [44] is applied to the constitutive equation, Equation (8), to stabilize convective momentum transport. This method has successfully been applied to find solutions for relatively high values of *De* and can be applied to a broader class of constitutive equations than those allowed with other FEMs based on stress splitting [34,35]. Applying the DEVSS-G FEM to the problem considered in this work, the governing equations of Section 2 take the following form:

$$\nabla \cdot \boldsymbol{T} = \alpha \nabla \cdot [G + G^T - (\nabla \boldsymbol{v} + \nabla \boldsymbol{v}^T)] \tag{17}$$

$$\nabla \cdot \boldsymbol{v} = 0 \tag{18}$$

$$\tau + De \overset{\nabla}{\tau} = G + G^T \tag{19}$$

$$G = \nabla v \tag{20}$$

$$\frac{\partial F}{\partial t} + \boldsymbol{v} \cdot \nabla F = 0 \tag{21}$$

where Equations (17) and (19) are the modified forms of Equations (6) and (8) respectively. Equation (20) is an identity for G. When a polymeric solution or purely Newtonian fluid is modeled, the solvent viscosity is non-zero ($p_s \neq 0$) in the Oldroyd-B constitutive law employed here, and no additional numerical stabilization is needed. For this case, the parameter α is set to zero. For the case of modeling the flow of a purely polymeric fluid (i.e. a polymer melt), the solvent viscosity is zero ($p_s = 0$), and regularization of the momentum equation is needed to preserve its ellipticity. Under these conditions, α is set to unity, and the difference between the discrete (discontinuous) approximation of the velocity gradient tensor, $\nabla \boldsymbol{v}$, and its continuous approximation, G, (obtained from a least-squares solution of Equation 20) is added numerically to the momentum balance via Equation (17).

3.1. Spatial discretization

The governing equations (17)–(21) are recast as the following strong-form weighted residual equations:

$$R^i_m = \int_\Omega \Phi^i \boldsymbol{e}_k \cdot (-\nabla \cdot \boldsymbol{T} + \alpha \nabla \cdot [G + G^T - (\nabla \boldsymbol{v} + \nabla \boldsymbol{v}^T)])\, d\Omega \tag{22}$$

$$R^i_c = \int_\Omega \varphi^i (\nabla \cdot \boldsymbol{v})\, d\Omega \tag{23}$$

$$R^i_f = \int_\Omega \bar{\Psi}^i \boldsymbol{e}_k \boldsymbol{e}_l : \left(\tau + \lambda \overset{\nabla}{\tau} - (G + G^T) \right) d\Omega \tag{24}$$

$$R_g^i = \int_\Omega \Psi^i \boldsymbol{e}_k \boldsymbol{e}_l : \ (G - \nabla \boldsymbol{v})\, \mathrm{d}\Omega \tag{25}$$

$$R_S^i = \int_\Gamma \zeta^i \left(\frac{\partial F}{\partial t} + \boldsymbol{v} \cdot \nabla F \right) \mathrm{d}\Gamma \tag{26}$$

where subscripts m, c, f, g and S refer to the momentum, continuity, fluid constitutive, velocity gradient and kinematic equations respectively. Superscript i refers to a node associated with the basis functions defined over the discretized domain. The integrals are taken over either the problem domain, $\Omega \in V_d \cup V_m$, or the free boundary, $\Gamma \in V_d \cap V_m$. The Φ^i, φ^i, Ψ^i and ζ^i are the basis functions for velocity, pressure, extra stress and velocity gradient, and boundary shape respectively.

The overbar on Ψ^i in Equation (24) reflects implementation of streamline upwinding [44] where

$$\bar{\Psi}^i = \Psi^i + h\boldsymbol{v} \cdot \nabla \Psi^i$$

The coefficient, h, is a constant over each element, evaluated to be proportional to the average dimension of the element as $h = (0.1)\ (\mathrm{Length}_{\mathrm{elem}} + \mathrm{Width}_{\mathrm{elem}})/2$.

The divergence of the total stress tensor, on the right-hand-side of Equation (22), is integrated by parts and the divergence theorem applied to yield weak-form residuals [45]. The boundary integral that results allows a direct substitution of the natural boundary conditions given by Equations (10) and (15). Direct evaluation of the second derivatives of drop surface shape, associated with the dimensionless mean curvature, κ, in Equation (10), are avoided by integrating the boundary integral by parts as described by Ruschak [46]. Essential boundary conditions for the velocity, Equation (14), are enforced along the symmetry planes.

Discrete approximations to the dependent variables are made using basis functions selected from the same function space as the test functions used to form the corresponding weighted residuals, i.e.

$$v_k = \sum_{j=1}^{N_1} v_{k,j} \Phi^j(\mathbf{x}) \tag{27}$$

$$p = \sum_{j=1}^{N_3} p_j \varphi^j(\mathbf{x}) \tag{28}$$

$$\tau_k = \sum_{j=1}^{N_2} \tau_{k,j} \Psi^j(\mathbf{x}) \tag{29}$$

$$G_k = \sum_{j=1}^{N_2} G_{k,j} \Psi^j(\mathbf{x}) \tag{30}$$

$$H = \sum_{j=1}^{N_H} H_j \zeta_j(\mathbf{x}) \tag{31}$$

Subscript k reflects the kth component of a vector or tensor. We choose to solve this particular problem in a spherical coordinate system (r, θ, ϕ) whose origin is defined at the drop center. For velocities, $k = r$ or θ; for extra stresses, $k = rr$, $r\theta$, $\theta\theta$ or $\phi\phi$; and for velocity gradients, $k = rr$, $r\theta$, θr, $\theta\theta$ or $\phi\phi$. The coefficients within the summations preceding the basis functions comprise the time-dependent unknowns.

A mixed set of basis (test) functions is chosen to ensure the LBB compatibility conditions [43]. Consistent with implementation of the DEVSS-G FEM as reported by Baaijens [34], piecewise-continuous, biquadratic polynomials (Φ^i) are chosen for velocities, and piecewise-continuous, bilinear polynomials (Φ^i) are used for the velocity gradients and extra stresses. Rather than using discontinuous, bilinear polynomials for pressure [34], we employ discontinuous, linear polynomials (φ^i), since these involve fewer pressure degrees of freedom and have been used quite successfully in Newtonian fluid flows [43]. Finally, piecewise-continuous, quadratic basis functions (ζ^i) are used to represent the drop boundary position, where the function defining the drop surface is represented as

$$F = r - H(\theta, t) \tag{32}$$

This representation is always single-valued in the co-ordinate system employed here and allows for simple interface tracking using the method of spines [47]. Corresponding to this choice of basis functions, N_1 represents the number of velocity nodes in the computational domain (nine per element), N_2 is the number of extra stress and velocity gradient nodes (four per element), N_3 is the number of pressure nodes (three *within* each element), and N_H represents the number of nodes defining the drop boundary (three per boundary element).

3.2. Viscoelastic fluid–fluid interface

An important implementation issue for this problem is pointed out by the force balance across the drop surface, Equation (10). Clearly, tangential stresses must be continuous; however, normal stresses are discontinuous at the surface due to the contributions of surface tension. Fortuitously, these requirements are easily satisfied for Newtonian fluids using standard Galerkin finite element discretizations. Important in these implementations is that only continuity of the velocity field is imposed by construction of the solution approximation, e.g. via Equation (27) above; the stress tensor of the Newtonian fluid is expressed in terms of pressure and velocity derivatives, both of which can be constructed to be discontinuous across element boundaries. For example, the normal stress jump is easily accommodated using piecewise-discontinuous pressure representations, and the continuity of tangential stresses is naturally satisfied by the stress-divergence weak form of the momentum equations. For the DEVSS-G formulation, employed here for viscoelastic fluids, the direct discretization of the extra stress tensor is required. While it may seem reasonable to allow the extra stress tensor components to be continuous across the interface, as the construction of Equation (29) implies, the requirements of the force balance stated by Equation (10) are not so stringent. In fact, forcing all components of the stress tensor to be continuous overspecifies the problem and can lead to significant difficulties. We demonstrate this formulation issue by comparing results obtained with the formulation of Equation (29), which implicitly forces continuity of all the

extra stresses across the interface, with the correct formulation, in which extra degrees of freedom are added to the discretization to allow for discontinuity of the extra stress and velocity gradient components at the drop interface. Figure 4 shows a comparison of the extra stress components along a mesh spine (θ fixed and r varying) for a viscoelastic drop deformation computation using both continuous and discontinuous extra stresses. The slight shift in values is due in part to the slightly different times at which the values were taken. Clearly noticeable is the presence of wiggles near the drop boundary ($r \approx 1.0$) when continuity is enforced for each extra stress component. The deleterious effects on drop deformation predictions are shown in Figure 5 for the same drop extension calculation. For continuous extra stresses, wiggles eventually produce oscillations in drop strain and lead to convergence failure at a very short time. When the stresses are allowed to be discontinuous across the drop boundary, drop deformation was smooth, and solutions were possible to very long times ($t > 3.5$). All ensuing results employ the formulation with discontinuous extra stresses and velocity gradients at the drop boundary.

3.3. Temporal discretization

The approximations in Equations (27)–(31) are substituted into the weak-form residual equations, which are then evaluated using 3×3-point Guassian quadrature, to yield a set of ordinary differential and algebraic equations (DAE) for the unknowns. Expressing the degrees of freedom compactly as a single unknowns vector, $\boldsymbol{y}$, allows the discretized system to be written as follows

$$\mathbf{M}\frac{\mathrm{d}\boldsymbol{y}}{\mathrm{d}t} = \mathbf{F}(\boldsymbol{y}) \tag{33}$$

where $\mathbf{F}$ consists of the steady state form of Equations (22)–(26), and $\mathbf{M}$ is the mass matrix containing the coefficients of the time derivatives. $\mathbf{M}$ is singular due to the absence of explicit time derivatives for the velocities, velocity gradients and pressure. To integrate this set of DAEs in time, we employ a fully implicit, second-order accurate trapezoid scheme [43]. When applied in conjunction with an Adams–Bashforth predictor, a variable time step based on the difference between the predictor and the actual solution leads to fewer time steps and a reduction in overall computation time. The time-dependence of the basis functions resulting from the deforming mesh is accounted for in a consistent manner as prescribed by Lynch [48]. The resulting system of non-linear equations is solved using Newton's method [49] and a direct banded matrix solver.

3.4. Boundary element method

The BEM is also used to solve the governing equations of this problem. We employ the method previously developed and applied by Toose *et al*. [26–28]. The interested reader should consult these references for details; only a brief overview of the method is presented here.

The BEM is formulated in terms of integral representations of the flow field; we assume the fluid to be Newtonian outside of the drop and viscoelastic (Oldroyd-B) inside the drop. A solution for the velocity at time t can be constructed in terms of boundary integral equations [50]. Following Ladyzhenskaya [51], the integral representation for the velocity is given by [28]

$$\boldsymbol{v}(\boldsymbol{x}) + (1 - p_s) \int_S \boldsymbol{n}:\ \boldsymbol{K}(\boldsymbol{v}(\boldsymbol{y}) - \boldsymbol{v}(\boldsymbol{x}))\, \mathrm{d}S_y = \boldsymbol{v}^{\infty}(\boldsymbol{x}) + \int_{V_d} \nabla \cdot \boldsymbol{\tau} \cdot \boldsymbol{J}\, \mathrm{d}y + \int_S \kappa \boldsymbol{n} \cdot \boldsymbol{J}\, \mathrm{d}S_y \tag{34}$$

where $\boldsymbol{x}$ denotes the spatial coordinates of the problem, $\boldsymbol{y}$ is a dummy variable of integration, and $\boldsymbol{J}$ and $\boldsymbol{K}$ are the Green's functions for the Stokes problem [50]

$$\boldsymbol{J} = \frac{1}{8\pi} \left\{ \frac{\boldsymbol{I}}{|\boldsymbol{r}|} + \frac{\boldsymbol{rr}}{|\boldsymbol{r}|^3} \right\}, \qquad \boldsymbol{K} = -\frac{3}{4\pi} \frac{\boldsymbol{rrr}}{|\boldsymbol{r}|^5}$$

with $\boldsymbol{r} = \boldsymbol{x} - \boldsymbol{y}$. Since the flow problem remains axisymmetric the dimension of the computational problem can be reduced by transforming Equation (34) to cylindrical co-ordinates [27]. The presence of the non-Newtonian stress, however, makes it impossible to reduce the problem to one dimension as is possible for a purely Newtonian drop [9]. This implies that the computational effort required to solve non-Newtonian problems is considerably higher than for corresponding Newtonian problems. However, only the volume of the drop needs to be discretized, since the outer fluid is assumed to be Newtonian.

The computations are carried out by defining a mesh of points along the surface of the drop S as well as a set of discrete collocation points in the internal domain V_d. The extra stresses and velocities are specified at these collocation points to permit computation of the viscoelastic response of the drop. At the start of the simulation, the extra stresses are initialized per Equation (16), and the corresponding velocity field is calculated using the boundary integral formulation. The time evolution of the non-Newtonian axisymmetric drop is carried out using an explicit, forward Euler scheme as follows: using the velocity given at time t and the evolution equation (12), the new positions of the collocation points are calculated to obtain the shape of the drop at $t + \Delta t$. Clustering of the moving boundary nodes at the drop surface is reduced by constraining their motion to the direction normal to the boundary; interior grid points are interpolated between the center axis and the new boundary position. Integrating Equation (8) in time yields and extra stress tensor at the new time level. With this new stress tensor and shape of the boundary, a new velocity field at time level $t + \Delta t$ can be calculated from Equation (34). At this point all of the information describing the state of the drop—the position of collocation points and the velocity and non-Newtonian stresses at these points—has advanced one time step. Repeating this explicit time integration procedure gives the evolution of the stress tensor, the velocity field, and the shape of the drop.

4. RESULTS

We carry out the FEM computations on a domain of finite extent, approximating a drop within an unbounded matrix. For most of the results discussed here, we apply the condition expressed in Equation (13) as a Dirichlet condition on the outer boundary of the matrix, which is given a circular shape and extends beyond the initial drop size by a factor of 10. We employ meshes of rectangular elements in (r, θ)-space with a typical mesh consisting of 16 elements in the radial dimension within the drop, 24 elements in the radial dimension within the matrix, and 24 elements in the angular dimension; this mesh is shown in Figure 2 and comprises a total

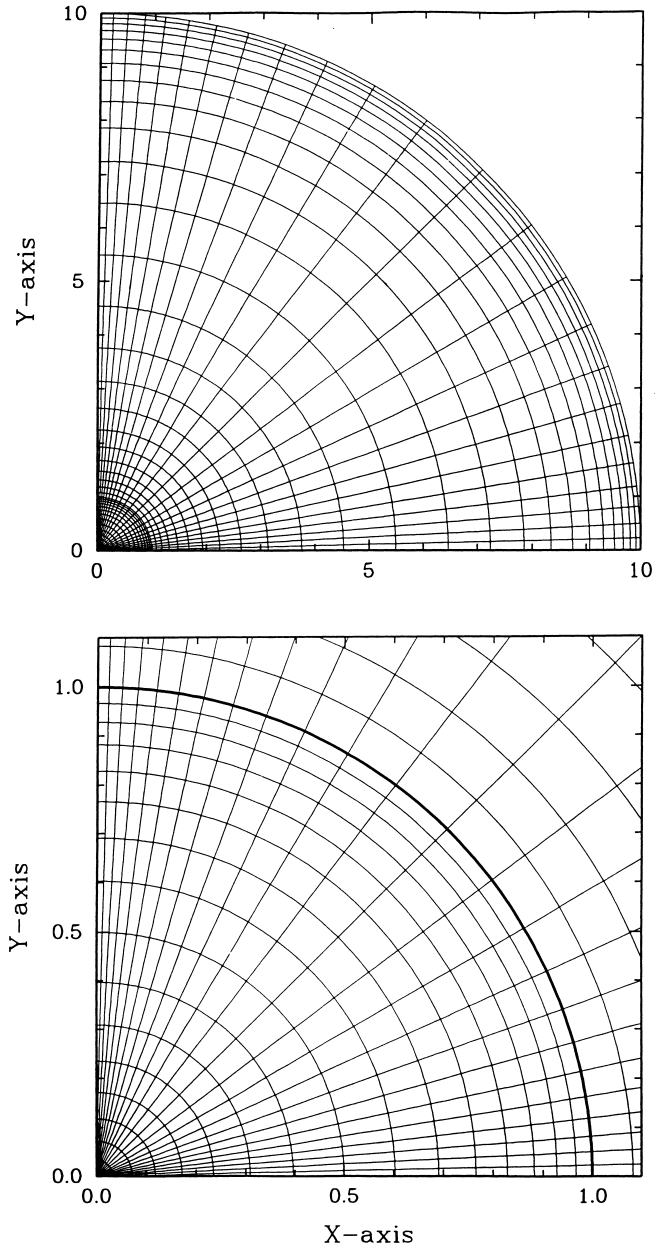

Figure 2. Typical mesh used for the FEM. (Top) The full mesh consists of $16 \times 24 \times 24$ (drop radial $\times$ matrix radial $\times$ angular) elements and represents 20415 degrees of freedom. The matrix extends 10 drop radii to approximate unboundedness. (Bottom) The drop is initially spherical and set to have unit radius. Grading is used in the drop and matrix domains.

of 20415 degrees of freedom. The meshes are graded toward the drop boundary, the outer matrix boundary, and the symmetry axes in order to resolve the steep velocity and stress gradients that can occur in these regions. Slightly more or less refined meshes were used to balance economy with accuracy, and mesh dimensions are given in the Figure captions. The implicit time integration used with the FEM does not impose any stability limits and easily allows variable time steps to be taken. Simulations were started with an initial time step $\Delta t = 10^{-4}$, and the error criterion for time step size adjustment was set to 10^{-3} [43]. Typically, on the order of 100 time steps were needed to reach a dimensionless time of $t = 2.0$. The convergence quality of this degree of spatial and temporal resolution and extent of matrix domain was established for a severe case as described in detail in Section 4.1.2.

The BEM employed here naturally satisfies the far-field boundary condition of Equation (13). In addition, owing to the Green's function formulation of the BEM, only the drop surface need be discretized for Newtonian fluids; consideration of a viscoelastic drop requires an interior discretization, as described previously. For the computations carried out in this study, we employ a mesh consisting of nine radial nodes and 32 angular nodes; see Figure 3. The time step size for the explicit integration scheme used with the BEM was constrained to ensure temporal stability. We employed a time step of $\Delta t = 0.005$, so 400 time steps were required to reach $t = 2.0$. Convergence characteristics of the BEM

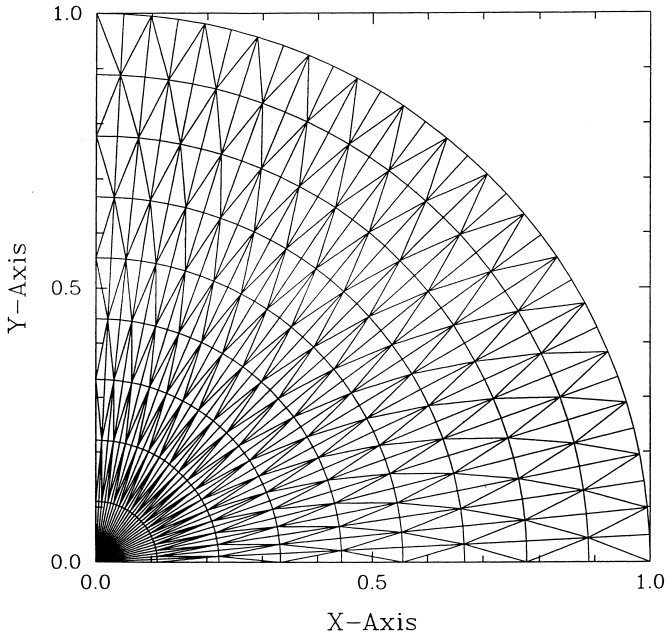

Figure 3. Typical mesh used for the BEM. The mesh of triangles has dimensions of 9×32 (radial $\times$ angular) elements.

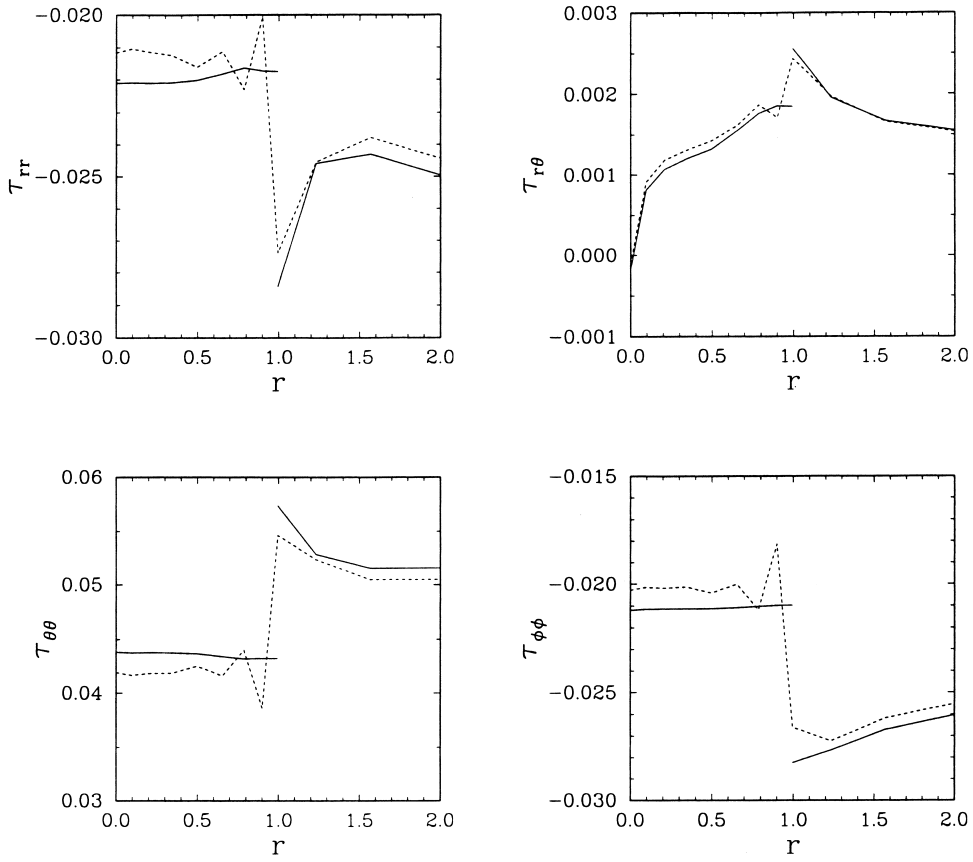

Figure 4. Extra stress components for UCM drop in UCM matrix with $p = 1.0$, $De_d = 0.1$, $De_m = 0.1$ and $Ca \to \infty$ at $t = 0.0075$ plotted versus radial position along the spine defined by $\theta = 90°$. Components that are continuous across the drop boundary are shown by dashed curves (---), and discontinuous components are shown as solid curves (—). A coarse mesh of $8 \times 8 \times 10$ elements (drop radial × matrix radial × angular) was used.

are discussed at length in [28]. We also address accuracy and convergence issues in Section 4.1.2.

The following sections present results obtained using the FEM and BEM described previously for the start-up uniaxial extension of a droplet. The purpose of this section is twofold: first, to compare the performance of the two methods and, second, to assess the physics of these flows, especially the effects of viscoelasticity. Both transient evolutions and steady states are assessed by considering both supercritical ($Ca > Ca_c$) and subcritical ($Ca < Ca_c$) flows under a number of different scenarios.

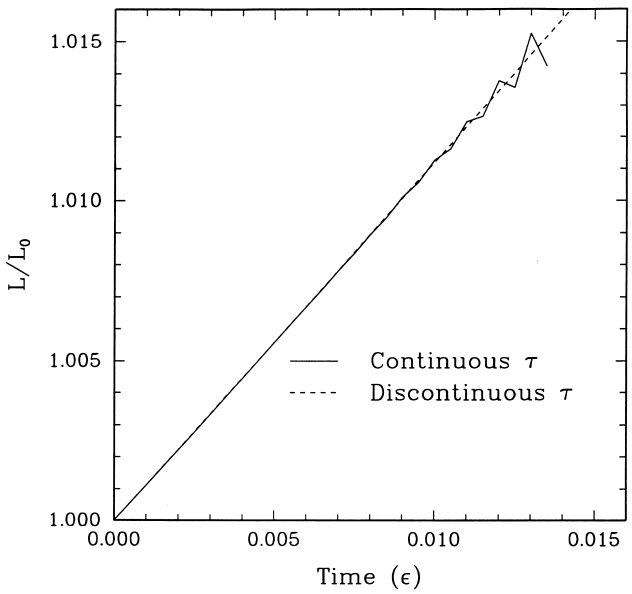

Figure 5. Drop strain, L/L_0, versus dimensionless time (Hencky strain of matrix fluid) for the UCM/UCM drop/matrix system of Figure 4.

4.1. Drops within a Newtonian matrix

Computing the dynamics of drops suspended within a Newtonian matrix is readily accomplished using either the FEM or the BEM. Here, we consider several scenarios and compare results predicted by both approaches.

4.1.1. Newtonian drops within a Newtonian matrix. To begin, a purely Newtonian system (drop/matrix) having no interfacial tension ($Ca \to \infty$) is considered. The only relevant rheological parameter in this case is the viscosity ratio, $p = \mu_d/\mu_m$. Figure 6 compares transient drop deformations for three different viscosity ratios predicted by the FEM and BEM with the linear theory (LT) of Delaby *et al.* [16], who employed small deformation theory to predict viscoelastic drop deformation in elongational flows. In the Figure, drop strain, L/L_0, is plotted as a function of dimensionless time, $t = \dot{\epsilon}t'$, or the Hencky strain of the matrix, ϵ [38]. Without interfacial tension, the drops reach no steady shape but instead deform passively. Very close agreement is observed for the three approaches in the time interval shown. The agreement for large drop deformations associated with $p = 0.5$ ($L/L_0 > 5$ at $t = 1.5$) reflects the ability of the FEM and BEM to handle significant mesh distortions.

Including sufficient interfacial tension so that $Ca < Ca_c$ leads to steady drop shapes at long times which reflect the balance between viscous and interfacial forces. In addition to the viscosity ratio, p, the capillary number, Ca, now plays a role. The critical capillary number falls between $0.10 < Ca_c < 0.15$ for a wide range of viscosity ratios in Newtonian systems. We

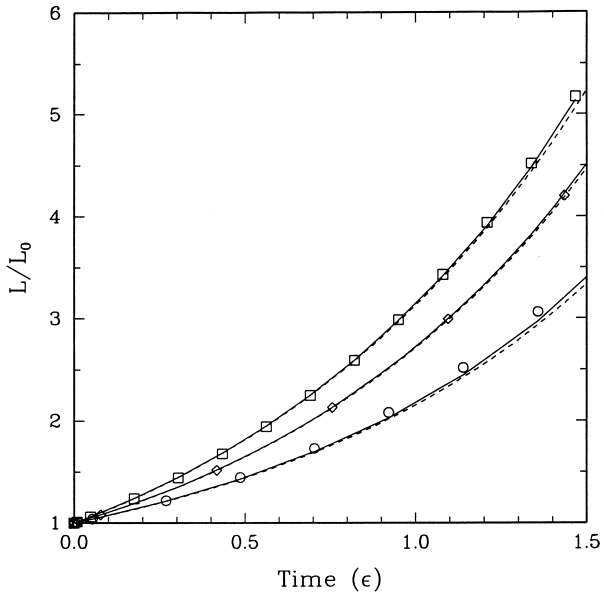

Figure 6. Drop strain, L/L_0, versus dimensionless time for Newtonian drop in Newtonian matrix with $Ca \to \infty$. Solid curves show FEM results, dashed curves show BEM results and symbols show results from LT for three viscosity ratios: (□) $p = 0.5$; (◇) $p = 1.0$; and (○) $p = 2.0$. The FEM mesh had $16 \times 24 \times 16$ elements, and the BEM mesh had 32 angular elements.

consider several combinations of capillary number and viscosity ratio in Figure 7. The capillary number is fixed at $Ca = 0.05$ for several values of the viscosity ratio in the computations represented in Figure 7(a)–(c). The viscosity ratio is set at unity, $p = 1.0$, while the capillary number is varied for the simulations shown in Figure 7(d)–(f). In all instances, the FEM and BEM results agree quite well for the entire drop deformation, and good agreement with linear theory is observed for the early stages of drop strain. However, linear theory consistently under predicts steady state deformation compared with the results from the non-linear numerical calculations. As might be expected from small-deformation analysis, the deviation between linear theory and the numerical predictions increases directly with the amount of drop deformation. For example, with $p = 1.0$, the $Ca = 0.025$, 0.05, and 0.10 curves of Figure 7(d)–(f) exhibit differences in steady-state L/L_0 of approximately 0.004, 0.02 and 0.14 with corresponding deviation percentages of 0.4, 1.8 and 10.3 respectively. Taken together, these results establish the accuracy and applicability of the FEM and BEM computations to predict the behavior of Newtonian systems and underscore the limitation of linear theory to accurately describe only small drop deformations.

4.1.2. Viscoelastic drops within a Newtonian matrix. Next, we consider the simulation of a polymeric drop described by the Oldroyd-B constitutive law within a Newtonian exterior flow. Figure 8 shows results for a drop Deborah number of $De_d = 1.0$, equal polymer and solvent

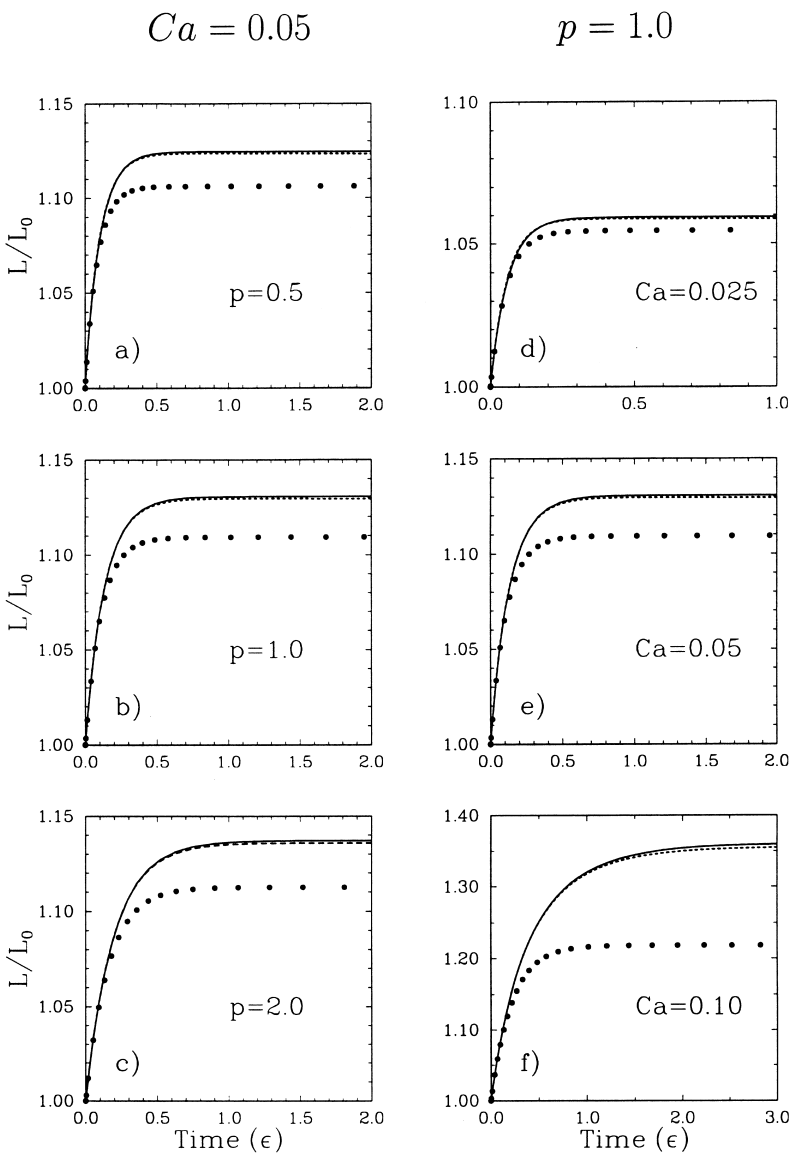

Figure 7. Drop strain, L/L_0, versus dimensionless time for Newtonian/Newtonian systems comparing FEM (—), BEM (---) and LT (●). Holding $Ca = 0.05$, viscosity ratios are compared: (a) $p = 0.5$; (b) $p = 1.0$; and (c) $p = 2.0$. Holding $p = 1.0$, different values of Ca are compared: (d) $Ca = 0.025$; (e) $Ca = 0.05$; and (f) $Ca = 0.10$. The FEM mesh had $16 \times 24 \times 16$ elements, and the BEM mesh had 32 angular elements.

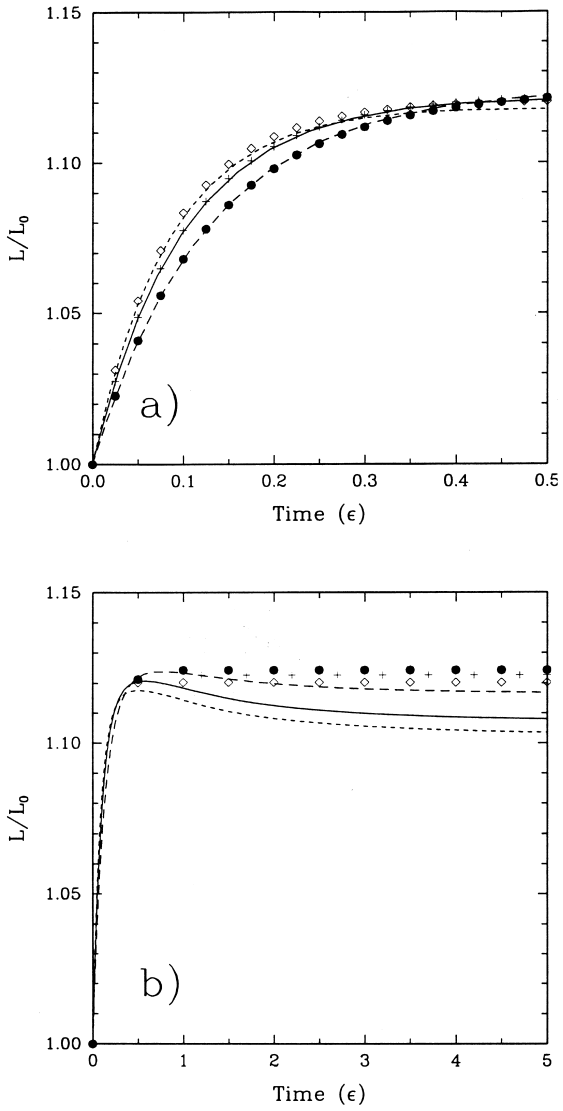

Figure 8. Drop strain, L/L_0, versus dimensionless time for Oldroyd-B drops in a Newtonian matrix having $p_{sd} = 0.5$ and $Ca = 0.05$. Curves are for FEM results: (---) $p = 0.5$; (—) $p = 1.0$; and (– – –) $p = 2.0$. Symbols are for BEM results: ($\diamond$) $p = 0.5$; (+) $p = 1.0$; and (●) $p = 2.0$. (a) and (b) differ only in the amount of time shown. A FEM mesh of $16 \times 24 \times 32$ elements and a BEM mesh of 9×32 elements were used.

contributions to the drop viscosity, i.e. $p_{sd} = p_{pd} = 0.5$, a subcritical capillary number of $Ca = 0.05$, and drop-to-matrix viscosity ratios of $p = 0.5$, 1.0 and 2.0. Results obtained with the FEM are shown via curves, and boundary element predictions are represented by symbols. Drop evolution over early times is shown in Figure 8(a) and very good agreement is obtained from the beginning of deformation to just before a steady state is reached at $t \approx 0.5$. The continuing evolution of drop length for the same cases at later times is shown in Figure 8(b). Interestingly, the FEM predicts an overshoot in drop strain prior to reaching steady state drop elongation, whereas the BEM shows the steady state to have been reached montonically.

This same trend is observed when the drop-to-matrix viscosity ratio is set to unity, $p = 1.0$, and the capillary number is varied between $Ca = 0.025$, 0.05 and 0.10, as shown in Figure 9. Finite element computations are represented by solid curves, while boundary element results are shown with dotted curves. Again, Figure 9(a) shows early times, during which both methods predict very similar results. As in the prior computations, long-term behaviors differ significantly; see Figure 9(b). At subcritical capillary numbers, the FEM predicts an overshoot in elongation prior to attaining the steady state, in contrast to the boundary element results, which show a monotonic approach to steady state. The difference between the two methods becomes even more pronounced when the critical capillary number is approached: Figure 9(b) shows that the BEM predicts the conditions at $Ca = 0.10$ to be supercritical, while the finite element results predict this condition to be subcritical.

To further examine the discrepancy between the predictions by these two methods, we repeated the finite element calculations for the $Ca = 0.10$ case under significantly increased levels of spatial and temporal refinement for much higher accuracy. Specifically, the meshing was increased from $16 \times 24 \times 32$ elements (radial dimension within the drop $\times$ radial dimension within the matrix $\times$ angular dimension) comprising a total of 27039 degrees of freedom to $24 \times 48 \times 70$ elements comprising a total of 103719 degrees of freedom, the error criterion for time step size selection in the trapezoid rule was reduced from 10^{-3} to 10^{-4}, and potential artifacts associated with upwind stabilization were removed from the new computation by setting $h = 0$ in Equation (24). The FEM computation using this fine mesh is compared with the original computation shown in Figure 9(b) for the $Ca = 0.10$ case in Figure 10. The resulting transient strain, L/L_0, for the fine-mesh calculation was at all times within 0.2 per cent of the original calculation. A similar refinement was made with the BEM for the $Ca = 0.10$ case in which the interior mesh of 9×32 points (radial $\times$ angular) was increased to 24×64 points and the time step size decreased from 0.005 to 0.002. These two computations are also shown in Figure 10. The transient strain computed using increased refinement for the BEM is shifted significantly closer to the that predicted by the FEM, although the BEM results still indicate this case to be supercritical. A detailed discussion on the discrepancy between the predictions by the two methods is presented in Section 5.

4.2. Drops within a viscoelastic matrix

In this section, we consider cases where the exterior fluid is viscoelastic. Such cases cannot be represented by the BEM employed here but are handled in a straightforward manner by the FEM.

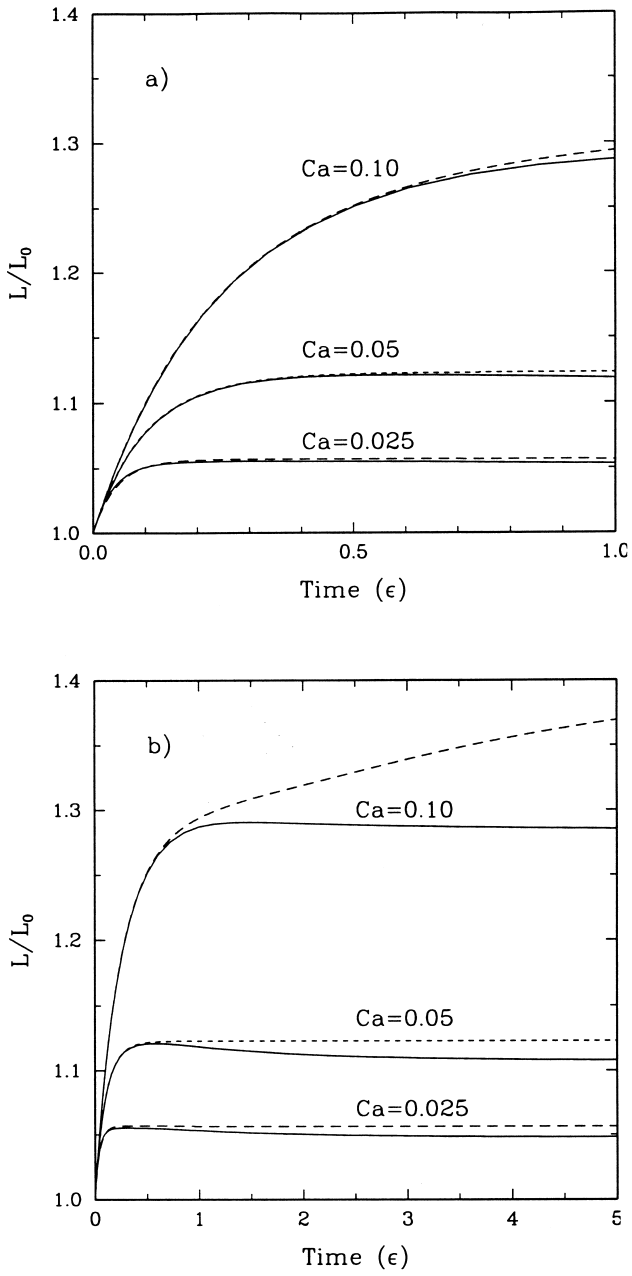

Figure 9. Drop strain, L/L_0, versus dimensionless time for Oldroyd-B drops in a Newtonian matrix having $p_{sd} = 0.5$ and $p = 1.0$. Solid curves (—) denote FEM results, and dashes curves (---) are BEM results. (a) and (b) differ in the amount of time shown. A FEM mesh of $16 \times 24 \times 32$ elements and a BEM mesh of 9×32 elements were used.

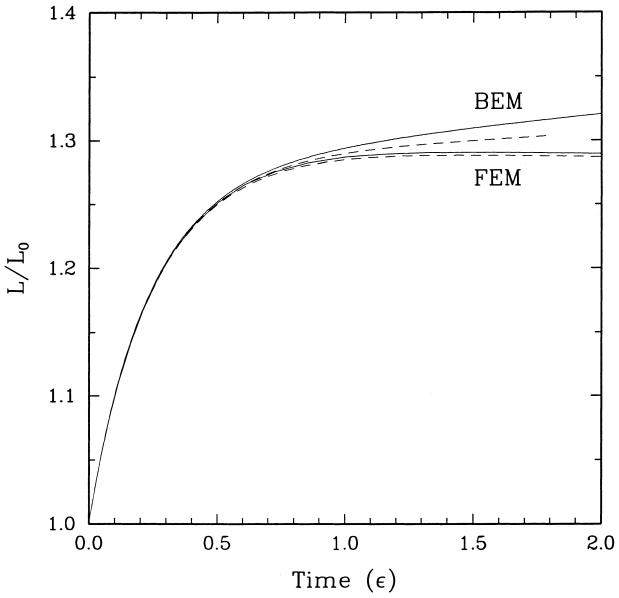

Figure 10. Drop strain, L/L_0, versus dimensionless time for the $Ca = 0.10$ results of Figure 9 at two mesh refinements. The solid curves (—) are the preceding results, and the dashed curves (---) have the following mesh dimensions: BEM (upper curve), 4×64; FEM (lower curve), $24 \times 48 \times 70$.

4.2.1. Newtonian drops within a viscoelastic matrix. In this section we consider the exterior matrix to be represented by an Oldroyd-B fluid with a Deborah number of $De_m = 0.1$. We consider equal polymer and solvent viscosities in this exterior phase, $p_{sm} = p_{pm} = 0.5$. The drop is Newtonian, with a drop-to-matrix viscosity ratio of $p = 1.0$ and a capillary number of $Ca = 0.10$.

Figure 11 shows the transient extension of this drop at short and long times, along with comparable results for a Newtonian matrix and for the reverse case of an Oldroyd-B drop ($De_d = 1.0$) in a Newtonian matrix. The latter two cases are the $p = 1.0$, $Ca = 0.10$ results of Figures 7 and 9 respectively. Figure 11(a) shows that viscoelasticity in the drop allows a faster initial rate of drop deformation than for a Newtonian drop of the same viscosity. Conversely, the drop deforms more slowly in a viscoelastic matrix, compared with the purely Newtonian case.

The steady state deformations shown in Figure 11(b) indicate that drop viscoelasticity suppresses the final deformation, while matrix viscoelasticity produces a greater deformation relative to the purely Newtonian case. As will be discussed at greater length in a subsequent paper [52], viscoelastic drops have the ability to store energy and thereby resist deformation. The enhanced deformation accompanying matrix viscoelasticity is attributed to the presence of normal forces, which squeeze the drop.

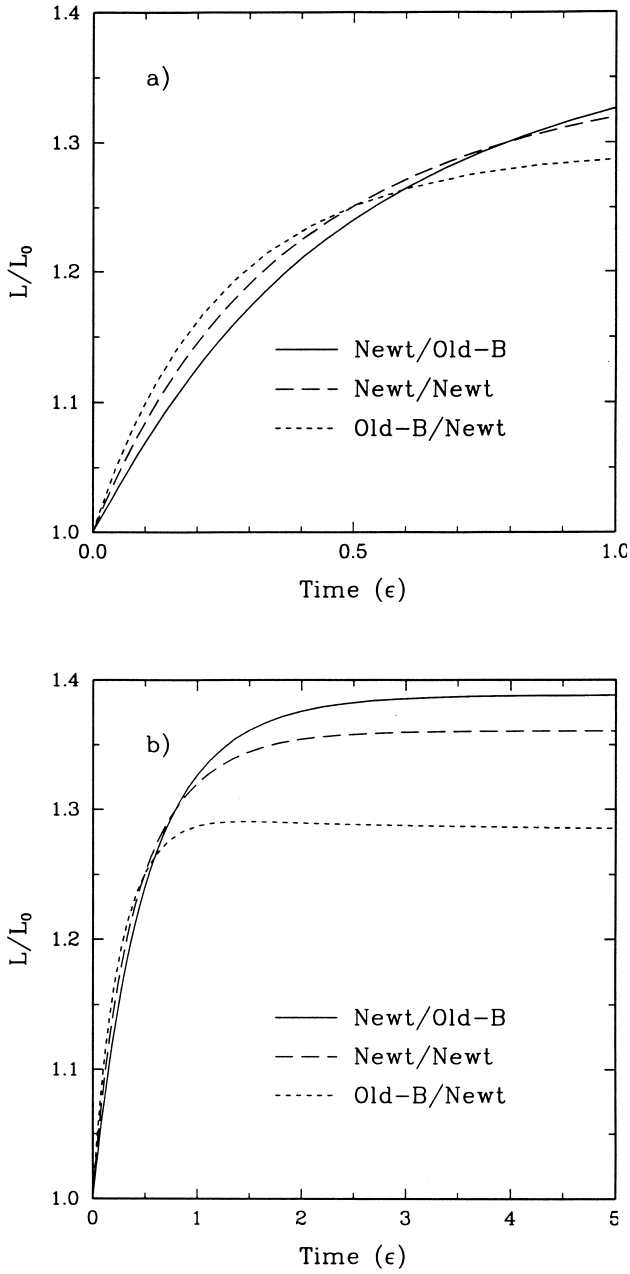

Figure 11. Drop strain, L/L_0, versus dimensionless time for systems with viscoelasticity in the drop only (---), the matrix only (—) or neither (– – –). Results are for FEM with $p = 1.0$ and $Ca = 0.10$. (a) and (b) differ in the amount of time shown. A mesh of $16 \times 24 \times 32$ elements was used.

4.2.2. Viscoelastic drop within a viscoelastic matrix. Finally, we briefly consider the case of a completely viscoelastic system, with polymeric drop and matrix. Here, we apply the UCM constitutive equation, obtained by setting the solvent viscosity to zero, $p_{sd} = 0$ and $p_{sm} = 0$, in the Oldroyd-B equation. Under such conditions, we regularize the momentum equation by setting $\alpha = 1.0$ in Equation (22).

Having already compared the FEM predictions with linear theory in Section 4.1.1 for Newtonian systems as the viscosity ratio p and capillary number Ca are varied, we now consider only the case of equal drop and matrix viscosities, $p = 1.0$, the limit of zero surface tension, $Ca \to \infty$, and several combinations of drop and matrix elasticity (represented via the De_d and De_m). Figure 12 shows drop strain versus time predicted by the FEM and linear theory as curves and symbols respectively. The drops elongate monotonically in the absence of interfacial tension, and the agreement between the finite element computations with linear theory is excellent early on but worsens with increasing deformation. Of particular interest is the case of $De_d = De_m = 1.0$. For equal elasticity and viscosity in the drop and matrix, the drop and matrix fluids are indistinguishable and, in the absence of interfacial tension, the drop deformation is governed by the flow kinematics for a homogeneous fluid undergoing uniaxial extension, i.e. $L/L_0 = e^{\epsilon}$. This relation is represented by the filled circles of Figure 12 which lie on the corresponding FEM curve, showing excellent agreement up to significant drop strains

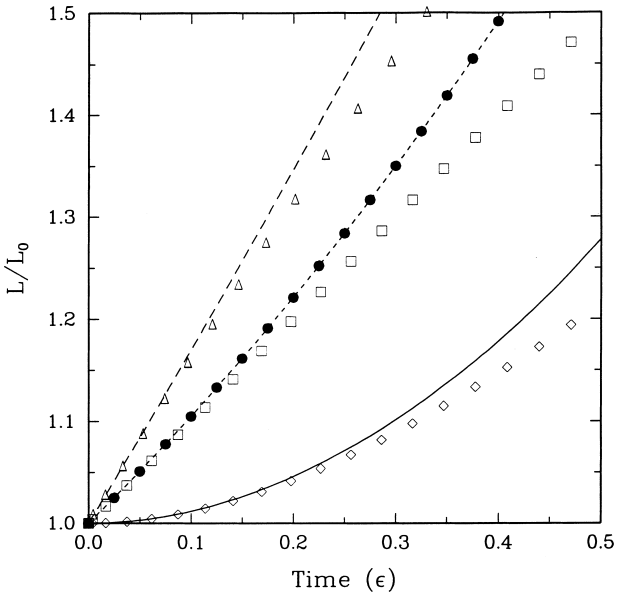

Figure 12. Drop strain, L/L_0, versus dimensionless time for UCM/UCM systems having $Ca \to \infty$ and $p = 1.0$. Curves are for FEM results: (—) $De_d = 0$, $De_m = 1.0$; (---) $De_d = 1.0$, $De_m = 1.0$; and (– – –) $De_d = 1.0$, $De_m = 0$. Open symbols show LT results: (◇) $De_d = 0$, $De_m = 1.0$; (□) $De_d = 1.0$, $De_m = 1.0$; and (△) $De_d = 1.0$, $De_m = 0$. Solid circles (●) are points on the curve $L/L_0 = e^{\epsilon}$. A mesh of $16 \times 24 \times 16$ was used.

(50 per cent). The open squares represent the predictions from linear theory; these points are intersected by the line (which is not shown in the figure), $L/L_0 = 1 + \epsilon$, which is simply the linear approximation to the actual exponential drop elongation.

As an interesting aside, the drop deformations for $p < 1.0$ in Newtonian systems and for $De_d/De_m > 1.0$ in UCM systems exhibit drop strains which exceed that of the matrix, i.e. $L/L_0 > e^{\epsilon}$. Hence, the curve in Figure 12 for $De_m = 0$ represents the upper limit of this phenomenon arising from elastic effects of a UCM drop.

5. DISCUSSION AND CONCLUSIONS

We have presented computations of drop deformation in start-up uniaxial extensional flows under different combinations of Newtonian and viscoelastic constitutitve behaviors. Our results provide a consistent comparison of the DEVSS-G FEM and the BEM of Toose *et al.* [26–28] and shed new insight into the behavior of this physical system.

Our calculations of Newtonian drops within a Newtonian matrix demonstrate that the FEM and BEM methods are consistent with each other and, under conditions of small drop deformation, consistent with the linear theory of Delaby *et al.* [16]. For such systems with no inertial effects (such as those of interest here), the BEM has a clear advantage over the FEM in terms of required computational effort. This arises since the Green's functions employed by the BEM allow for an exact mapping of the two-dimensional domain of the problem onto the one-dimensional surface of the drop. The BEM computations presented here were readily performed on a modest engineering workstation, while the FEM required substantially more memory and one to two orders of magnitude greater processing time.

The BEM retains some of these advantages for modeling a viscoelastic drop within a Newtonian matrix. Modifying the BEM to account for a polymeric drop requires the introduction of collocation points within the drop to assess the stress field of the viscoelastic fluid, negating some of the advantages of reducing the dimensionality of the problem as occurs for a purely Newtonian system. With its interior collocation points, the BEM employed here is similar in spirit to the FEM with its meshing of the drop interior. On the other hand, the BEM does not appear to suffer from the difficulties posed to the FEM by the high Weissenberg problem. While the DEVSS-G FEM used in this work has allowed for the computation of flows with higher values of elasticity, an upper limit of De still exists [34]. The BEM has the ability to obtain solutions in the limit, $De \to \infty$, and has even been used to study deformations of fully elastic particles [27]. In general, the BEM is expected to provide solutions up to the limits of a given fluid consitutive model, whereas the FEM will likely fail sooner as a result of numerical problems related to the high Weissenberg problem. Explicit time integration in the BEM saves on memory requirements and obviates solving linear equations at each time step (as required during the Newton iteration in the trapezoid rule in the FEM), thus speeding time step computations, but imposes time step size limits for numerical stability.

Following the discussion of the above paragraph, for the typical discretizations employed here, the modified BEM was approximately one order of magnitude faster than the FEM in terms of required processing time. However, the discrepancies between predictions of long-time behavior presented in Section 4.1.2 are a cause for concern. For the discretizations employed

here, the BEM predicted qualitatively different bahaviors than those exhibited by the corresponding FEM computations; notably the BEM did not predict extensional overshoot of the viscoelastic drop and predicted supercritical behavior at $Ca = 0.10$ where the FEM predicted subcritical behavior. The $Ca = 0.10$ case is particularly challenging to compute, since large stress gradients develop near the drop tips to balance the drop and matrix stress fields at steady state (see, for example, the results presented in Reference [52]). We believe that the BEM computations are not as accurate as the FEM computations, as evidenced by the convergence behaviors shown in Figure 10. While the BEM calculations at the higher level of discretization approach those of the FEM, the results differ qualitatively on the issue of criticality. We believe that the $Ca = 0.10$ case is indeed subcritical and that the discretization error of the modified BEM is to blame for its prediction of supercritical drop extension. We specifically suspect that the mesh placement strategy of the BEM is inadequate to accurately resolve this difficult calculation. At each time step, the new positions of the interior nodes are found by interpolating from the updated boundary position to the drop center [27]. This remeshing could serve to smooth the stress fields slightly. Given that time integration is performed explicitly and therefore requires relatively many small time steps, even very small amounts of smoothing introduced by remeshing could produce significant effects at later times. Alternatively, the uniform placement of interior nodes may simply be inadequate to resolve the steep stress boundary layers near the steady state. We also believe that the overshoot behavior exhibited by the other cases is directly related to such stress boundary layers [52] and that the effects of smoothing or under-resolution would preclude their prediction by the BEM. Interestingly, the fine-mesh BEM computation required over two orders of magnitude longer processing time than the original-mesh BEM computations, thus making the computational effort of the fine-mesh BEM greater than the original-mesh FEM computations (which are accurate, as demonstrated in Figure 10). It is quite conceivable that, to achieve an adequate level of mesh refinement where viscoelasticity and stress boundary layers play an important role in drop deformation, the commanding computational advantages held by the BEM over the FEM would be significantly diminished or even eliminated.

An indisputable advantage of the FEM over the BEM is its flexibility, such as the ability to predict incompressible flows with inertia, and, as demonstrated here, the ability to predict flows of any combination of viscoelastic or Newtonian fluids. The computations of Section 4.2 demonstrate the effects of a viscoelastic matrix on the drop extension problem. When the matrix fluid is viscoelastic, relatively slower initial drop deformation rates are predicted, and the presence of normal stresses in the matrix produces larger steady state drop deformations. A more thorough investigation of the effects of drop and matrix viscoelasticity on drop deformation in uniaxial flows will be presented in a forthcoming publication [52].

ACKNOWLEDGMENTS

This work was supported in part by the Army High Performance Computing Research Center under the auspices of the Department of the Army, Army Research Laboratory cooperative agreement DAAH04-95-2-0003/contract DAAH04-95-C-0008, the content of which does not necessarily reflect the position or policy of the government, and no official endorsement should be inferred. MT expresses his thanks of CWM and his colleagues for the opportunity to conduct this study during a short period in residence at the University of Minnesota.

REFERENCES

1. Subramanian PM, Mehra V. Laminar morphology in polymer blends: Structure and properties. *Polymer Engineering and Science* 1987; **27**: 663–668.
2. Lohfink GW, Kamal MR. Morphology and permeability in extruded polypropylene/ethylene vinyl-alcohol copolymer blends. *Polymer Engineering and Science* 1993; **33**: 1404–1420.
3. Lee SY, Kim SC. Morphology and oxygen barrier properties of LDPE/EVOH blends. *International Polymer Processing* 1996; **XI**(3): 238–247.
4. Taylor GI. The viscosity of a fluid containing small drops of another fluid. *Proceedings of the Royal Society* 1932; **A138**: 41–48.
5. Cox RG. The deformation of a drop in a general time-dependent fluid flow. *Journal of Fluid Mechanics* 1969; **37**: 601–623.
6. Barthès-Biesel D, Acrivos A. Deformation and burst of a liquid droplet freely suspended in a linear shear field. *Journal of Fluid Mechanics* 1973; **61**: 1–21.
7. Brunn PO. The deformation of a viscous particle surrounded by an elastic shell in a general time-dependent linear flow field. *Journal of Fluid Mechanics* 1983; **126**: 533–544.
8. Stone HA, Leal LG. Breakup on concentric double emulsion droplets in linear flows. *Journal of Fluid Mechanics* 1990; **211**: 123–156.
9. Rallison JM. The deformation of small viscous drops and bubbles in shear flows. *Annual Review of Fluid Mechanics* 1984; **16**: 45–66.
10. Stone HA. Dynamics of drop deformation and breakup in viscous fluids. *Annual Review of Fluid Mechanics* 1994; **26**: 65–102.
11. Oldroyd JG. The elastic and viscous properties of emulsions and suspensions. *Proceedings of the Royal Society* 1953; **A218**: 122–132.
12. Oldroyd JG. The effects of interfacial stabilizing films on the elastic and viscous properties of emulsions. *Proceedings of the Royal Society A* 1955; **232**: 567–577.
13. Palierne JF. Linear rheology of viscoelastic emulsions with interfacial tension. *Rheologica Acta* 1990; **29**: 204–214.
14. Palierne JF. Erratum: Linear rheology of viscoelastic emulsions with interfacial tension. *Rheologica Acta* 1991; **29**: 497.
15. Delaby I, Ernst B, Germain Y, Muller R. Droplet deformation in polymer blends during uniaxial elongational flow: Influence of viscosity ratio for large capillary numbers. *Journal of Rheology* 1994; **38**(6): 1705–1720.
16. Delaby I, Ernst B, Muller R. Drop deformation during elongational flow in blends of viscoelastic fluids. small deformation theory and comparison with experimental results. *Rheologica Acta* 1995; **34**: 525–533.
17. Delaby I, Ernst B, Froelich D, Muller R. Droplet deformation in immiscible polymer blends during transient uniaxial elongational flow. *Polymer Engineering and Science* 1996; **36**: 1627–1635.
18. Roscoe R. On the rheology of a suspension of viscoelastic spheres in a viscous liquid. *Journal of Fluid Mechanics* 1967; **28**: 273–293.
19. Jeffery GB. The motion of ellipsoidal particles immersed in a viscous fluid. *Proceedings of the Royal Society A* 1922; **102**: 161–179.
20. Youngren GK, Acrivos A. Stokes flow past a particle of arbitrary shape: A numerical method of solution. *Journal of Fluid Mechanics* 1975; **69**: 377–403.
21. Tjahjadi M, Stone HA, Ottino JM. Satellite and subsatellite formation in capillary breakup. *Journal of Fluid Mechanics* 1992; **243**: 297–317.
22. Stone HA, Leal LG. The effects of surfactants on drop deformation and breakup. *Journal of Fluid Mechanics* 1990; **220**: 161–186.
23. Li XZ, Barthes-Biesel D, Helmy A. Large deformations and burst of a capsule freely suspended in an elongational flow. *Journal of Fluid Mechanics*. 1988; **187**: 179–196.
24. Li X, Charles R, Pozrikidis C. Simple shear flows of suspensions of liquid drops. *Journal of Fluid Mechanics* 1996; **320**: 395–416.
25. Loewenberg M, Hinch EJ. Numerical simulation of a concentrated emulsion in shear flow. *Journal of Fluid Mechanics* 1996; **321**: 395.
26. Toose EM, van Damme RMJ, van den Ende HTM, Geurts BJ, Kuerten JMG. A boundary element method for two-dimensional (non)-Newtonian drops in slow viscous flow. *Journal of Non-Newtonian Fluid Mechanics* 1995; **60**: 129–154.
27. Toose EM, van den Ende D, Geurts BJ, Kuerten JGM. Axisymmetric non-Newtonian drops treated with a boundary integral method. *Journal of Engineering and Mathematics* 1996; **30**: 131–150.
28. Toose EM. Simulation of the deformation of non-Newtonian drops in a viscous flow. PhD thesis, University of Twente, The Netherlands, 1997.

29. Ramaswamy S. Study of inertial and viscoelastic effects on drop deformation. PhD thesis, Department of Chemical Engineering, University of California, Santa Barbara, CA, 1997.
30. Ramaswamy S, Leal LG. The deformation of a viscoelastic drop subjected to steady uniaxial extensional flow of a Newtonian fluid. *Journal of Non-Newtonian Fluid Mechanics* 1999; **85**: 127–163.
31. Keunings R. An algorithm for the simulation of transient viscoelastic flows with free surfaces. *Journal of Computational Physics* 1986; **62**: 199–220.
32. Janssen J. Dynamics of liquid–liquid mixing. PhD thesis, Eindhoven University of Technology, The Netherlands, 1993.
33. Bousfield DW, Keunings R, Denn MM. Transient deformation of an inviscid inclusion in a viscoelastic extensional flow. *Journal of Non-Newtonian Fluid Mechanics* 1988; **27**: 205–221.
34. Baaijens FPT. Mixed finite element methods for viscoelastic flow analysis: a review. *Journal of Non-Newtonian Fluid Mechanics* 1998; **79**: 361–385.
35. Guenette R, Fortin M. New mixed finite element method for computing viscoelastic flows. *Journal of Non-Newtonian Fluid Mechanics* 1995; **60**(1): 27–52.
36. Bird RB, Stewart WE, Lightfoot EL. *Transport Phenomena*. Wiley: New York, 1965.
37. Bird RB, Armstrong RC, Hassager O. *Dynamics of Polymeric Liquids* (2nd edn), vol. 1. Wiley: New York, 1987.
38. Macosko CW. *Rheology Principles, Measurements, and Applications*. VCH Publishers: New York, 1994.
39. Levich VG. *Physicochemical Hydrodynamics*. Prentice-Hall: Englewood Cliffs, NJ, 1962.
40. Segel LA. *Mathematics Applied to Continuum Mechanics*. Dover: New York, 1969.
41. Joseph DD, Renardy M, Saut JC. Hyperbolicity and change of type in the flow of viscoelastic fluids. *Archives of Rational Mechanical Analysis* 1985; **87**: 213–251.
42. Joseph DD, Saut JC. Short-wave instabilities and ill-posed initial-value problems. *Theoretical and Computational Fluid Dynamics* 1990; **1**: 191–227.
43. Gresho PM, Sani RL. *Incompressible Flow and the Finite Element Method*. Wiley: New York, 1998.
44. Brooks AN, Hughes TJR. Streamline upwind/Petrov–Galerkin formulations for convection dominated flows with particular emphasis on the incompressible Navier–Stokes equations. *Computer Methods in Applied Mechanics and Engineering* 1982; **32**: 199–259.
45. Reddy JN. *An Introduction to the Finite Element Method*. McGraw-Hill: New York, 1984.
46. Ruschak KJ. A method for incorporating free boundaries with surface tension in finite element fluid-flow simulators. *International Journal for Numerical Methods in Engineering* 1980; **15**: 639–648.
47. Kistler SF, Scriven LE. Coating flow theory by finite element and asymptotic analysis of the Navier–Stokes system. *International Journal for Numerical Methods in Fluids* 1984; **4**: 207–229.
48. Lynch DR. Unified approach to simulation on deforming elements with application to phase change problems. *Journal of Computational Physics* 1982; **47**: 387–411.
49. Asaithambi NS. *Numerical Analysis: Theory and Practice*. Saunders College Publishing: New York, 1995.
50. Lorentz HA. Eene algemeene stelling omtrent de beweging eener vloeistof met wrijving en eenige daaruit afgeleide gevolgen. *Versl K Akad W Amsterdam* 1896; **5**: 168–175.
51. Ladyzhenskaya OA. *The Mathematical Theory of Viscous Incompressible Flow*. Gordon and Breach: New York, 1969.
52. Hooper RW, DeAlmeida VF, Macosko CW, Derby JJ. Transient polymeric drop extension and retraction in uniaxial extensional flows. *Journal of Non-Newtonian Fluid Mechanics* 2001; **98**: 141–168.

